Nanometer-Thick Yttrium Iron Garnet Films with Perpendicular Anisotropy and Low Damping

Jinjun Ding,[1,†] Chuanpu Liu,[1,†] Yuejie Zhang,[1,2,†] Uppalaiah Erugu,[3] Zhiyong Quan,[4] Rui Yu,[1,5] Ethan McCollum,[1] Songyu Mo,[1] Sheng Yang,[1] Haifeng Ding,[5] Xiaohong Xu,[4] Jinke Tang,[3] Xiaofei Yang,[2] and Mingzhong Wu[1,*]

[1] *Department of Physics, Colorado State University, Fort Collins, Colorado 80523, USA*

[2] *School of Optical and Electronic Information, Huazhong University of Science and Technology, Wuhan, Hubei 430074, China*

[3] *Department of Physics and Astronomy, University of Wyoming, Laramie, Wyoming 82071, USA*

[4] *School of Chemistry and Materials Science and Key Laboratory of Magnetic Molecules and Magnetic Information Materials, Shanxi Normal University, Linfen, Shanxi 041004, China*

[5] *National Laboratory of Solid State Microstructures and Department of Physics, Nanjing University, Nanjing, Jiangsu 210093, China*

(Received 25 March 2020; accepted 4 June 2020; published 7 July 2020)

$Y_3Fe_5O_{12}$ (YIG) thin films having a thickness of several nanometers and showing both strong perpendicular magnetic anisotropy (PMA) and low magnetic damping are reported. The films are deposited by magnetron sputtering at room temperature first and then annealed in O_2 at high temperature. The substrates are $Gd_3(Sc_2Ga_3)O_{12}$, which share the same crystalline structure as YIG, but have a lattice constant slightly larger than that of YIG; the lattice mismatching gives rise to an out-of-plane compressive strain and PMA in the YIG films. The PMA is confirmed by vibrating sample magnetometer, magneto-optical Kerr effect, anomalous Hall effect, and angle-dependent ferromagnetic resonance (FMR) measurements. The damping of the films is analyzed through frequency-dependent FMR measurements. As an example, an 8-nm-thick YIG film shows an effective PMA field of about 2800 Oe, a nearly square hysteresis loop, and a damping constant of only 4.2×10^{-4}. As an illustration of possible applications of such films in spintronic devices, current-induced switching of the magnetization of the PMA YIG films is demonstrated by the use of YIG/Pt bilayered Hall bar devices.

DOI: 10.1103/PhysRevApplied.14.014017

I. INTRODUCTION

Magnetic thin films with perpendicular anisotropy manifest themselves as core components in a wide variety of electronic devices that range from hard disk drives [1], to magnetic-tunnel-junction- (MTJ) based sensors [2,3], to spin-transfer-torque (STT) memory [4,5], to racetrack memory [6], to spin-torque nano-oscillators (STNOs) [7,8], and to spin-wave logics [9]. For magnetic films in such applications, perpendicular magnetic anisotropy (PMA) is essential because it dictates the thermal stability, reliability, scalability, density, and/or compatibility of the devices. On the other hand, low damping is also essential for many of those applications. To give a few examples, the critical current for switching in STT memory is proportional to the damping constant (α) in PMA films; the speed of domain-wall motion in racetrack memory is generally inversely proportional to α; the threshold current for auto-oscillations in STNOs scales with α; and the spin-wave decay rate in spin-wave logic devices increases with α. As such, it is of great technological significance to search for magnetic thin films that exhibit (1) PMA and (2) low damping.

In terms of magnetic damping, yttrium iron garnet (YIG) is probably the most interesting material—α in YIG single crystals can be as low as 3×10^{-5}, which is lower than in any other known magnetic materials [10,11]. However, YIG thin films unfortunately do not show PMA; magnetocrystalline anisotropy in YIG materials is weaker than most magnetic materials. Nevertheless, several recent works suggest that one can realize PMA in YIG thin films through substrate lattice mismatching-induced epitaxial strain [12–15]. In fact, two of those works even succeeded in the realization of YIG thin films in which PMA is so strong that the hysteresis loops are nearly square [14,15]. Those works, though intriguing and enlightening, reported no results about the damping properties of the YIG films. Demonstration of YIG thin films that are nm thick, show

*mwu@colostate.edu

†These authors contributed equally to this work.

PMA, and exhibit low damping simultaneously are still awaiting.

This paper reports nm-thick YIG thin films with both PMA and low damping. The YIG films, with a thickness range of 4–30 nm, are deposited by magnetron sputtering at room temperature first and then annealed in O_2 at high temperature. The substrates are $Gd_3(Sc_2Ga_3)O_{12}$, which share the same crystalline structure as YIG but have a lattice constant slightly larger than that of the YIG, resulting in an out-of-plane compressive strain and a PMA in the YIG film. The PMA is confirmed by vibrating sample magnetometer (VSM), magneto-optical Kerr effect (MOKE), anomalous Hall effect (AHE), and angle-dependent ferromagnetic resonance (FMR) measurements. The damping of the films is analyzed through frequency-dependent FMR measurements. As an example, an 8-nm-thick YIG film shows an effective PMA field of about 2800 Oe, a square-like hysteresis loop with a remnant-to-saturation magnetization ratio of 98%, and a damping constant of about 4.2×10^{-4}. As an illustration of possible applications of such films, current-induced magnetization switching of PMA YIG films is demonstrated using YIG/Pt bilayered devices.

II. FILM GROWTH AND CHARACTERIZATION

The YIG films are grown on single-crystal (111) gadolinium scandium gallium garnet $Gd_3(Sc_2Ga_3)O_{12}$ (GSGG) substrates by radio-frequency sputtering. The lattice constant of the GSGG substrates is about 12.554 Å at room temperature. This constant is slightly larger than the lattice constant in YIG materials, which is 12.359 Å at 4 K, 12.361 Å at 77 K, and 12.376 Å at 273 K [11]. This lattice mismatching is crucial for the realization of PMA in the YIG films, as discussed shortly. The GSGG substrates are rinsed sequentially with acetone, isopropyl alcohol, and DI water, before being loaded into the sputtering chamber. A commercial YIG target is used, which has a diameter of 2 inches and a thickness of 0.25 inches. The deposition is carried out at room temperature, at a rate of about 0.94 nm/min; before sputtering, the chamber has a base pressure of 2.0×10^{-8} Torr. The as-deposited YIG films are amorphous. To realize the crystalline structure, they are annealed in O_2 at high temperature in a separate chamber. The major sputtering and postannealing control parameters are summarized in Table I. More information about the sputtering and postannealing processes can be found in Refs. [16,17].

As control samples, YIG thin films are also grown on single-crystal (111) gadolinium gallium garnet $Gd_3Ga_5O_{12}$ (GGG) substrates. The GGG substrates have a lattice constant (12.382 Å) very close to that in YIG materials, so they are the most common substrates for YIG film growth.

For the YIG films presented in this paper, the surface morphological properties are analyzed through tapping-mode atomic-force-microscopy (AFM) measurements. The crystalline structure is characterized through x-ray-diffraction (XRD) measurements. The film thicknesses are determined through x-ray reflectivity (XRR) and ellipsometry measurements.

TABLE I. Sputtering and postannealing control parameters for YIG-film fabrication.

Sputtering	Target-to-substrate distance	4.8 cm
	Sample-holder rotation rate	10 rpm
	Ar pressure	20 mTorr
	Ar flow	4 sccm
	Sputtering power	80 W
	Sputtering time	4–13 min
Annealing	Heating rate	5 °C/min
	O_2 pressure	25 Torr
	Annealing temperature	900 °C
	Annealing time	180 min
	Cooling rate	2 °C/min

The static magnetic properties of the YIG films are measured by a VSM and a polar MOKE system. They are also examined through electric transport measurements on a Hall bar device made of a YIG/Pt bilayered structure. The dynamic properties of the films are determined through (1) polar angle-dependent FMR measurements using an X-band rectangular microwave cavity with a resonance frequency of 9.5 GHz and (2) frequency-dependent FMR measurements using a broadband vector network analyzer FMR (VNA FMR) spectrometer. For (1), field modulation and lock-in detection techniques are used to increase the sensitivity of the FMR measurements. For (2), a coplanar waveguide (CPW) is used to provide microwave magnetic fields to the YIG films.

III. PMA CHARACTERIZATION THROUGH STATIC MEASUREMENTS

This section and Sec. IV describe the use of static and dynamic measurements, respectively, to characterize the PMA properties of the YIG films grown on GSGG substrates. Figure 1 shows representative hysteresis responses of the PMA YIG films. The first row presents the data obtained on a 6-nm-thick YIG film with three different measurement techniques. Specifically, graphs (a) and (b) show the data obtained with a VSM system, graph (c) presents the data measured with a polar MOKE system, and graph (d) gives the AHE resistivity data obtained with a YIG/Pt Hall bar structure. The second row presents the data measured with the same technique, namely, the VSM method, but on four YIG films of different thicknesses, as indicated. During the measurements, an external static magnetic field (H) is applied in the film plane for the data in graph (a), but is applied out-of-plane for the data shown in all other graphs.

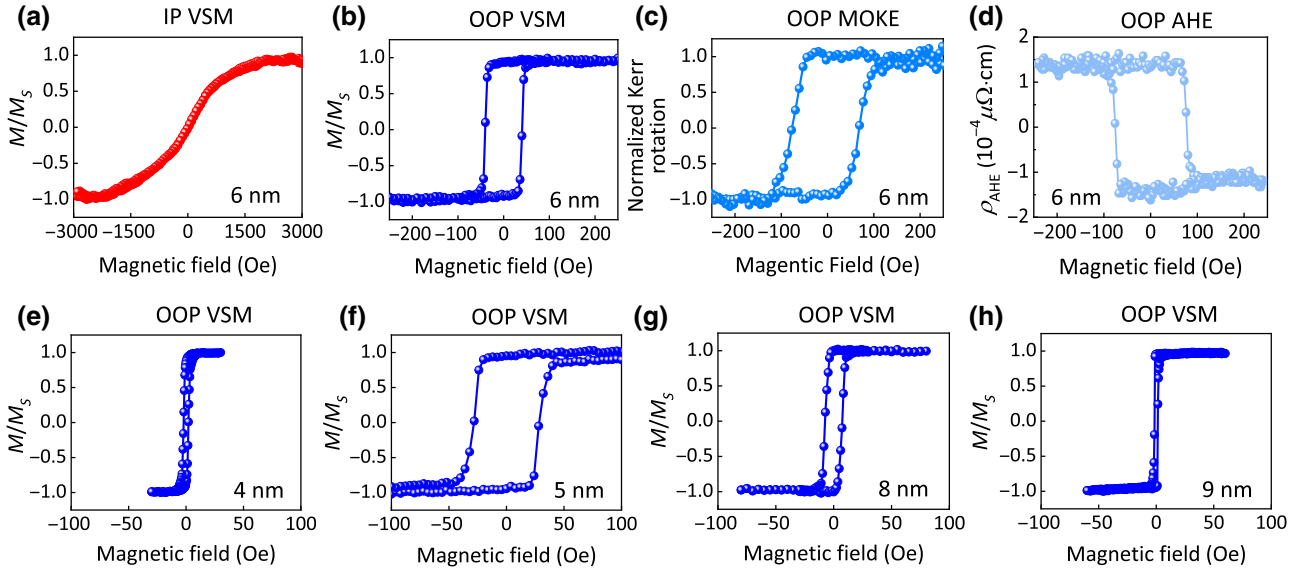

FIG. 1. Magnetic hysteresis responses of YIG thin films grown on GSGG substrates. (a), (b), (c), and (d) show the hysteresis responses measured on a 6-nm-thick YIG film. The data in (a) and (b) are measured by a VSM under an IP field and an OOP field, respectively. (c) and (d) show the MOKE data and the AHE resistivity data, respectively, both measured with OOP fields. (e), (f), (g), and (h) show the VSM data measured with OOP fields on YIG films of different thicknesses, as indicated. Note that the data in (d) are measured with a YIG/Pt Hall bar structure.

The VSM data in graphs (a) and (b) clearly show that (1) the magnetization is relatively hard to saturate when the field is in plane (IP) but is much easier when the field is out of plane (OOP); (2) the coercive field ($H_c \approx 4$ Oe) is close to zero for the IP configuration; (3) the hysteresis loop is nearly square and shows a very high remnant-to-saturation magnetization ratio ($M_r/M_s \approx 97\%$) for the OOP configuration. These results are typical responses of magnetic thin films with PMA and thereby evidently confirm the presence of the PMA in the YIG film.

Turn now to the comparison of three hysteresis loops in graphs (b), (c), and (d), which were obtained on the same 6-nm film in the same field configuration but with different techniques. Five important results are evident. (1) The data all show squarelike loops with near 100% M_r/M_s ratios. Thus, the presence of PMA in the 6-nm YIG film is confirmed by three completely distinct measurement techniques. (2) The data in graph (b) are measured on a sample with a dimension of 10×10 mm^2, the MOKE data in graph (c) are obtained with a laser-beam size of about 8 μm, and the AHE data in graph (d) are collected with a Hall bar structure that had a bar width of 10 μm. In spite of this size difference, the hysteresis loops are similar to each other, which indicates that the presence of the PMA is independent of the sample dimension. (3) The MOKE technique probes the entire thickness of the YIG film, while the AHE measurement examines only the magnetization at the YIG/Pt interface, as explained shortly. The consistency of the MOKE and AHE hysteresis loops indicates no major differences between the PMA in the bulk and that on the surface. (4) The comparison of the MOKE and AHE loops suggests that the growth of a Pt layer on top did not result in a notable degradation of the PMA in the YIG film. (5) From the VSM, MOKE, and AHE data, one can estimate H_c values to be 42, 73, and 76 Oe, respectively. One can see that the values from the MOKE and AHE loops agree with each other, but they are larger than the VSM value. This observation correlates with the sample size relation mentioned above. Specifically, the MOKE and AHE measurements are carried out on film areas (about $10 \times 10\,\mu$m^2) substantially smaller than the samples used in the VSM measurements (about 10×10 mm^2). Because of this considerable difference in the sampling area, the magnetic domain nucleation processes in the MOKE and AHE measurements can be different from those in the VSM measurements, giving rise to a difference in the H_c values.

It is worth highlighting that the above-presented results about the independence of the PMA from the film lateral dimension, the consistency between the bulk and surface properties, and the robustness of the PMA against the growth of a heavy-metal capping layer are important in terms of device applications of PMA YIG thin films.

It should also be explained that the AHE response usually occurs only in ferromagnetic metals and the AHE in the Pt layer of the YIG/Pt structure may originate (1) from the magnetic proximity effect, namely, magnetic ordering in the Pt layer induced due to the proximity to the YIG layer [18], (2) by the effects of the imaginary part of the spin-mixing conductance at the interface [19], or (3) due

to the spin-dependent scattering of itinerant electrons in the Pt layer with the magnetic interface [20]. One can write the Hall resistivity in the Pt layer as

$$\rho_H = \rho_{\mathrm{OHE}} + \rho_{\mathrm{AHE}} = R_0 H + R_a M, \tag{1}$$

where ρ_{OHE} denotes the ordinary Hall effect (OHE) resistivity in the Pt layer, M is the magnetization in the YIG film, and R_0 and R_a are constants. For the data shown in graph (d), the ρ_{OHE} component, scaling linearly with H, has already been subtracted. From Eq. (1), one can see that the ρ_{AHE} vs H loop can evolve in the same or opposite manner as the M-H loop, depending on the sign of R_a. The opposite evolution of the AHE and MOKE loops shown in Fig. 1 clearly indicates that R_a is negative in the YIG/Pt structure, which is consistent with the previous reports on the AHE responses in YIG/Pt [18,21] and $Tm_3Fe_5O_{12}$/Pt [22,23] bilayered structures. Note that the data in graph (d) are measured at room temperature. The AHE resistivity loop can show an opposite evolution at low temperature, as reported previously [18].

Graphs (b), (e), (f), (g), and (h) present the hysteresis loops measured with the same technique, namely, the VSM, under the same field, namely, an OOP field, for five YIG films with different thicknesses (t), as indicated. The data clearly indicate that PMA and the resulting squarelike loop exist in YIG films with a thickness ranging from 4 to 9 nm. Although not shown, the loop evolves gradually from a nearly square shape with a M_r/M_s ratio of 64.4% to a well tilted or sheared shape with a M_r/M_s ratio of only 0.3% when the film thickness t is increased from 10 to 30 nm. This evidently shows the degradation of the PMA with an increase in t. The reason for this degradation is discussed in Sec. V.

The analyses of the VSM data, such as those shown in Fig. 1, can yield the H_c, saturation induction $4\pi M_s$, and effective PMA field H_k values of the YIG films. Table II lists such values for eight samples. The first column gives the nominal thickness values (t) of the YIG films, which are determined through the XRR and ellipsometry measurements. The second column lists the $4\pi M_s$ values estimated from the saturation magnetic moments obtained from the VSM measurements under OOP fields. The estimation assumes a 2-nm-thick interfacial layer with zero moments at the YIG/GSGG interfaces. This "dead" layer results from the interfacial diffusion of Y^{3+} ions in the YIG film and Gd^{3+} ions in the substrate. As Y^{3+} ions have no magnetic moments but Gd^{3+} ions do, the substitution of Y^{3+} by Gd^{3+} in this interfacial layer can result in antiferromagnetic coupling between the magnetization in this layer and that in the YIG bulk, as studied previously through magneto-optical spectroscopy [24], neutron reflectivity [25,26], and energy-dispersive x-ray spectroscopy measurements [27]. The interfacial layer thickness reported previously ranges from about 1 to 7 nm; such a wide range may result from the use of different YIG film growth conditions. For the YIG films in this work, the estimation of the dead-layer thickness (2 nm) is based on polarized neutron reflectometry measurements of the depth dependence of both the structure and the magnetism in the YIG films [28].

TABLE II. Static magnetic properties of PMA YIG thin films.

Thickness (nm)	$4\pi M_s$ (G)	H_k (Oe)	H_c (Oe)
4	1206 ± 11	2556 ± 16	2.5 ± 0.4
5	1243 ± 8	2443 ± 14	28 ± 0.8
6	1218 ± 6	3428 ± 17	42 ± 1.6
7	1319 ± 9	2819 ± 16	32 ± 1.6
8	1427 ± 4	2827 ± 11	7.5 ± 0.8
9	1491 ± 8	2741 ± 12	1.5 ± 0.4
10	1663 ± 12	2263 ± 21	5.0 ± 0.4
12	1758 ± 13	2058 ± 25	0.3 ± 0.1

The third column in Table II lists the H_k values evaluated according to

$$H_s = H_k - 4\pi M_s = \frac{2K_u}{M_s} - 4\pi M_s, \tag{2}$$

where H_s is the saturation field for the IP configuration and can be obtained from the IP VSM loops such as the one shown in Fig. 1(a). K_u in Eq. (2) is the anisotropy constant and is described in detail in Sec. V. The last column in Table II gives the H_c values obtained from the OOP hysteresis loops, including those shown in Figs. 1(b) and 1(e)–1(h).

Note that each $4\pi M_s$ value in Table II is obtained by simply averaging the $4\pi M_s$ values measured with the positive and negative fields, while the corresponding error bar is the difference of the two $4\pi M_s$ values divided by two. The H_k and H_c values and the corresponding errors are obtained with the same method.

Three main results are evident from the data in Table II. First, the $4\pi M_s$ value of the 12-nm YIG film almost perfectly agrees with that of the bulk value in YIG crystals, which is 1750 G, but the values for the thinner films are smaller than the bulk value; a general trend is present in which $4\pi M_s$ decreases with a decrease in t. These observations indicate that the very thin films have low quality, possibly due to lattice mismatching and diffusion at the interfaces, and the film quality is gradually improved as t increases from 4 to 12 nm.

Second, the 6-nm YIG film shows the highest H_k, and H_k becomes smaller if t is either smaller or larger. This response likely results from the coexistence of two distinct effects: with an increase in t, the film quality becomes better as evident from the $4\pi M_s$ data in the second column, while the PMA becomes weaker due to strain relaxation, as discussed in Sec. V. In other words, H_k is relatively small in very thin films (4–5 nm) because of the low film quality

and is also small in relatively thick films (10–12 nm) due to the strain relaxation.

Third, the H_c data show the exact same trend as the H_k data, namely, that H_c is the largest for the 6-nm film and decreases if t is either reduced or increased. This consistency supports the validity of the observed H_k properties; in PMA films H_k generally dictates the domain nucleation and domain-wall motion processes and thereby determines H_c.

IV. PMA CHARACTERIZATION THROUGH FMR MEASUREMENTS

Figure 2 presents the FMR data that further support the above-presented results on the PMA properties of the YIG films. The data are measured with a 9.5-GHz rectangular cavity on a 10-nm-thick YIG film for different field angles (θ_H) relative to the film normal direction. Graph (a) shows a representative FMR profile measured at $\theta_H = 30°$. The blue circles show the data, while the red curve shows a numerical fit to the derivative of a Lorentzian trial function. The fitting yields the field ($H_{\rm FMR}$) and peak-to-peak linewidth ($\Delta H_{\rm pp}$) of the FMR. At certain field angles, the FMR profiles consist of multiple resonances, rather than a well-defined single resonance; for such profiles, the fitting is carried out only for the narrow central portion of the main resonance. Graphs (b) and (c) show $H_{\rm FMR}$ and $\Delta H_{\rm pp}$, respectively, as a function of θ_H, which are obtained from the Lorentzian fitting. The red curve in graph (b) shows a fit to [29,30]

$$\left(\frac{f}{|\gamma|}\right)^2 = [H_{\rm FMR}\cos(\theta_H-\phi_M)+(H_k-4\pi M_s)\cos(2\phi_M)] \times [H_{\rm FMR}\cos(\theta_H-\phi_M) + (H_k-4\pi M_s)\cos^2(\phi_M)], \quad (3)$$

where $|\gamma|$ is the absolute gyromagnetic ratio, and ϕ_M is the angle of the equilibrium magnetization relative to the film normal direction that can be found according to

$$H_{\rm FMR}\sin(\theta_H-\phi_M)-\frac{1}{2}(H_k-4\pi M_s)\sin(2\phi_M)=0. \quad (4)$$

The fitting yields $H_k = 2234.8 \pm 3.3$ Oe and $|\gamma| = 2.80$ MHz/Oe.

One can see two important results from the data in Fig. 2. First, the fitting-yielded H_k value (2235 Oe) is consistent with the corresponding value (2263 Oe) in Table II. This consistency evidently confirms the presence of the PMA in the film. Second, one has $\Delta H_{\rm pp} \leq 10$ Oe at low field angles. This suggests that the film has relatively low damping. The detailed discussions about the damping properties are presented in Sec. VI.

In addition, one can also see that $\Delta H_{\rm pp}$ increases with θ_H, which is likely due to the presence of two-magnon scattering in the YIG film. It is known that for magnetic thin films, two-magnon scattering is prohibited when $\theta_H = 0$, because of lacking degenerated spin-wave modes at the FMR frequency ($\omega_{\rm FMR}$), but occurs and contributes to $\Delta H_{\rm pp}$ when θ_H is nonzero and degenerated spin waves are present at $\omega_{\rm FMR}$ [31–34]. In principle, one can numerically fit the data in graph (c) to determine the contributions to $\Delta H_{\rm pp}$ from the intrinsic damping and the two-magnon scattering process. Such an analysis, however, is not carried out in consideration of the presence of multiple FMR peaks for some field angles and the error bars being relatively large.

Two notes should be made about the data presented in Fig. 2. First, FMR measurements with microwave cavities are usually expected to yield FMR profiles with large signal-to-noise ratios (SNRs), but the data in Fig. 2(a) appear to have a relatively small SNR. Possible reasons for this include the relatively low Q factor of the cavity and the aging of the diode detector used in the FMR measurements. Second, the presence of multiple FMR peaks is likely due to spatial inhomogeneity of the magnetic properties of the YIG films produced during the sputtering and annealing processes or induced by the strain.

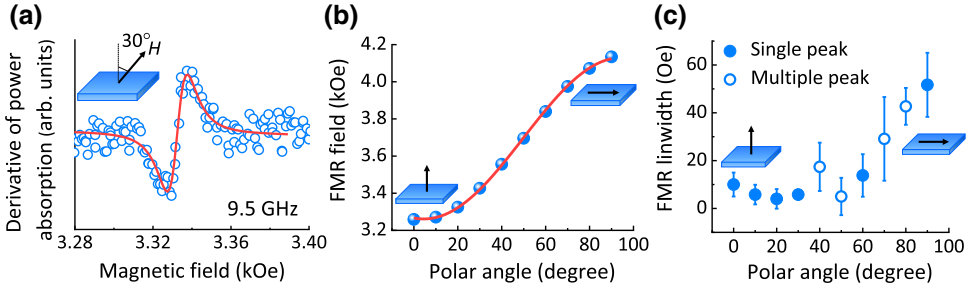

FIG. 2. Polar angle (θ_H)-dependent FMR on a 10-nm-thick YIG film grown on a GSGG substrate. (a) An FMR profile measured at $\theta_H = 30°$. (b) FMR field as a function of θ_H. (c) FMR linewidth as a function of θ_H. The red curve in (a) is a fit to the derivative of a Lorentzian trial function. The red curve in (b) is a fit to Eq. (3).

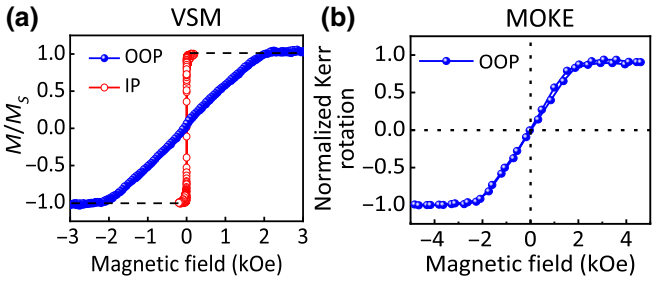

FIG. 3. Magnetic hysteresis responses of a 6-nm-thick YIG film grown on a GGG substrate. (a) VSM data measured under an OOP field and an IP field. (b) Polar MOKE data measured under an OOP field.

V. ORIGIN OF PMA

The above-presented PMA originates from strain-induced magnetoelastic anisotropy, as discussed in Refs. [12–15]. Specifically, because the lattice constant of YIG materials ($a_{\mathrm{YIG}} = 12.376$ Å) is smaller than that of GSGG substrates ($a_{\mathrm{GSGG}} = 12.554$ Å), there exists a tensile strain in the (111) plane of a (111) YIG thin film grown on a (111) GSGG substrate. This IP tensile strain corresponds to an OOP compressive strain if one assumes that the volume of the YIG unit cells is conserved. Such interfacial lattice mismatching-produced strain can induce a perpendicular, uniaxial magnetoelastic anisotropy in the YIG film that can be described by [35]

$$K_u = \frac{3}{2}\lambda_{111}\sigma, \tag{5}$$

where K_u is the anisotropy constant, λ_{111} is the magnetostriction constant along the (111) direction of the YIG, and σ is the uniaxial stress along the normal direction of the YIG film. Note that $\sigma > 0$ and $\sigma < 0$ correspond to a tensile stress and a compressive stress, respectively. The OOP compressive strain in the YIG films in this work gives rise to $\sigma < 0$. On the other hand, it is known that YIG materials have $\lambda_{111} = -2.4 \times 10^{-6}$ [14,15,36]. Thus, K_u is positive according to Eq. (5), and PMA is present in the YIG films grown on the GSGG substrates.

Figures 3 and 4 present experimental data that support the above interpretation about the physical origin of the PMA in the YIG films. Figure 3 gives the VSM and MOKE data measured on a 6-nm-thick YIG film that is grown under the exact same conditions as the 6-nm YIG film cited in Fig. 1 and Table II, but on a single-crystal (111) GGG substrate, rather than a GSGG substrate. The data show that the YIG film is much easier to magnetize for the field IP configuration than for the field OOP configuration. Further, the data for the OOP configuration show $H_c \approx 0.8$ Oe and $M_r/M_s \approx 0.3\%$, both substantially smaller than the corresponding values shown by the data in Fig. 1(b). These results are typical for YIG thin films grown on GGG substrates in which the lattice constants of the film and the substrate almost match each other, and lattice mismatching-produced strain is negligible. The comparison of the data in Fig. 3 with those in Figs. 1(a)–1(c) evidently confirm that the substrate, rather than the growth condition or the film thickness, plays a critical role in the formation of the above-described PMA. Note that the field IP VSM data yield $4\pi M_s \approx 1722$ G, which is close to the bulk value of the YIG (1750 G).

Figure 4(a) presents the XRD spectra for five YIG thin films grown on GSGG substrates as well as a bare GSGG substrate. In each spectrum, the two main peaks are for the (444) peaks of the GSGG substrate. The appearance of the two (444) peaks results from the coexistence of the $K_{\alpha 1}$ and $K_{\alpha 2}$ components of the x ray. The vertical dashed line indicates the position or angle expected for the (444) peak of YIG crystals, while the short arrows indicate the actual positions of the (444) peaks of the YIG films.

The comparison of the spectra in Fig. 4(a) indicates that the YIG (444) peaks of the films appear on the right side of the dashed line. This result indicates the presence of an OOP compressive strain in the YIG films according to Bragg's law for the XRD

$$2d\sin\vartheta = n\lambda, \tag{6}$$

where d is the spacing between diffracting planes parallel to the film plane, θ is the incident angle of the x ray, n is an integer, and λ is the wavelength of the x ray. An OOP compressive strain gives rise to a smaller d, while a decrease in d leads to an increase in θ, according to Eq. (6). In other words, a vertical compressive strain results in the appearance of the diffraction peak on the right side of the theoretical peak position.

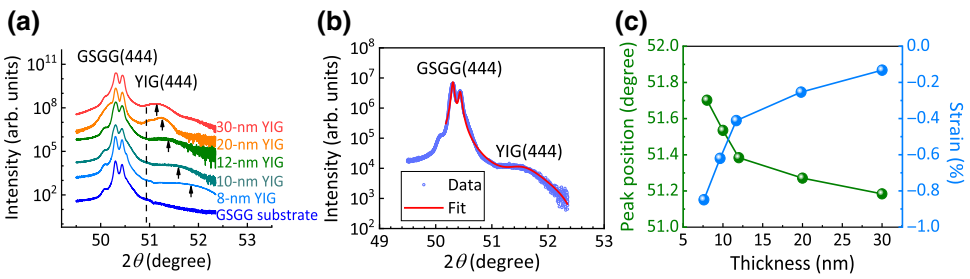

FIG. 4. (a) X-ray spectra of YIG thin films grown on GSGG substrates. (b) X-ray spectrum of a 10-nm YIG film (blue circles) and its numerical fit (red curve). (c) Angles of (444) peaks (left axis) and out-of-plane strain (right axis) of YIG thin films grown on GSGG substrates.

The comparison of the XRD spectra in Fig. 4(a) also shows that the thicker the YIG film is, the closer the (444) peak is to the dashed line. This observation indicates that an increase in the film thickness gives rise to a weaker strain in the film. This result is consistent with the interfacial nature of the lattice mismatching-produced strain; such a strain relaxes partially as the film becomes thicker.

In fact, one can also use the XRD data in Fig. 4(a) to determine the (444) peak positions (2θ) of the YIG films and thereby estimate the strain (ε) in the YIG films. Figure 4(b) shows the numerical fitting of the XRD spectrum of the 10-nm-thick YIG film. The red curve is a profile that consists of three Voigt functions, one for the YIG (444) peak and the other two for the GSGG (444) peaks; the fitting yields $2\theta \approx 51.54°$ for the 10-nm film. Through such fitting, one can obtain 2θ values for all the YIG films.

Figure 4(c) presents the 2θ and ε values. The green symbols show 2θ as a function of the film thickness (t), while the blue symbols show the ε values as a function of t, evaluated according to

$$\varepsilon = \frac{d - d_0}{d_0} = \frac{\sin\vartheta_0 - \sin\vartheta}{\sin\vartheta}, \tag{7}$$

where d_0 and θ_0 are the spacing and the peak position, respectively, expected for bulk YIG crystals. One can see that ε is negative, confirming the compressive nature of the strain in the YIG films. One can also see that the amplitude of ε decreases with an increase in t. This result, together with Eq. (5), suggests that the PMA in the YIG film should become weaker if t is increased. This trend is consistent with the overall trend shown in Table II, namely, that both H_k and H_c decrease when t is increased from 6 to 12 nm.

Three notes should be made about the above discussions. First, in addition to the magnetoelastic anisotropy described by Eq. (5), the YIG thin films are also expected to exhibit cubic magnetocrystalline anisotropy. For YIG crystals, the cubic anisotropy constants are $K_1 = -6100$ erg/cm^3 and $K_2 = -260$ erg/cm^3 [11]. For a (111)-oriented YIG film, such a crystalline anisotropy gives rise to an easy-axis anisotropy along the film normal direction that can be described by an effective anisotropy field

$$H_k = \frac{2|K_1|}{M_s} + \frac{4|K_2|}{M_s}. \tag{8}$$

If one takes the 6-nm YIG film as an example and uses the $4\pi M_s$ value presented in Table II, one obtains an anisotropy field of about 135 Oe, which is only about 4% of the corresponding H_k value in Table II. Thus, strictly speaking H_k in Eqs. (2) and (3) has two origins, a strain-induced magnetoelastic anisotropy and an intrinsic magnetocrystalline anisotropy, but the latter is substantially smaller than the former and is therefore neglected in the analyses described in Secs. III and IV. The magnetocrystalline anisotropy is also neglected in the discussions in the following sections for the same reason.

Second, in spite of the strong dependence of ε, H_k, and H_c on t, all the PMA YIG films show smooth surfaces, with a rms surface roughness range of 0.11–0.13 nm. This result is important from the point of view of applications of PMA YIG thin films in spintronic devices. Figure 5 presents representative AFM images obtained on films of different thicknesses, as indicated. The roughness values given in the figure are obtained by averaging over AFM measurements on five different $5 \times 5\,\mu$m^2 areas on the YIG film, while the uncertainty for each roughness value is the corresponding standard deviation. One can see that the films all show smooth surfaces.

Finally, it should be mentioned that in the XRD spectra shown in Fig. 4(a) the YIG (444) peaks appear as broad, weak humps on the right shoulder of the strong GSGG (444) peaks. Those YIG peaks are clearly defined for thicker films (20–30 nm), are less defined for thinner films (8–12 nm), and cannot be detected for very thin films (4–6 nm). Future work is of interest that makes use of high-resolution XRD measurements and reciprocal space-mapping analyses or high-resolution scanning transmission electron microscopy measurements to confirm the crystalline structure and analyze the strain properties in ultrathin PMA YIG films.

VI. DAMPING PROPERTIES

The dynamical properties of the PMA YIG films are determined through broadband VNA-based FMR measurements. Figure 6 shows the measurement and analysis

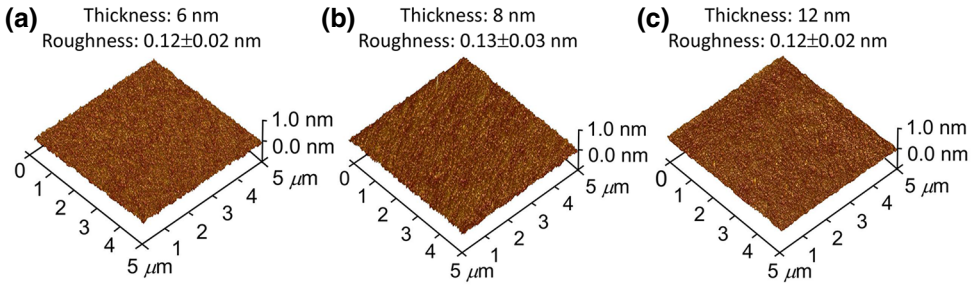

FIG. 5. Atomic force microscopy surface images of YIG thin films of different thicknesses, as indicated. The films are grown on GSGG substrates.

approaches. Figure 6(a) sketches the experimental setup, which consists mainly of a VNA and a CPW. The CPW structure has a 50-μm-wide signal line and a signal line-to-ground spacing of 25 μm; its nominal impedance is 50 Ω. The PMA YIG sample, shown as a red disk in Fig. 6(a), is placed on the CPW with the YIG-film side facing the CPW structure and the GSGG-substrate side facing up. An external static magnetic field (H), shown as a blue arrow in Fig. 6(a), is applied perpendicular to the film plane to either magnetize the YIG film to saturation or enable VNA FMR measurements.

The major measurement and data-analysis procedures are as follows:

(i) Magnetize the YIG film to saturation with a large perpendicular magnetic field. For the data presented below, this field is 5 kOe.

(ii) Measure the transmission coefficient (S_{21}) of the CPW/YIG structure as a function of H at a fixed microwave frequency (f). Figure 6(b) presents representative S_{21} profiles measured on an 8-nm-thick YIG film at $f = 14$ GHz.

(iii) Fit the S_{21} data with the theoretical S_{21} profiles [37,38] to determine the FMR field ($H_{\rm FMR}$) and the FMR linewidth (ΔH). The curves in Fig. 6(b) show such fits. Note that ΔH here refers to "full width at half maximum," rather than the peak-to-peak linewidth cited in Sec. IV.

(iv) Repeat (i)−(iii) for different microwave frequencies over 7–26 GHz.

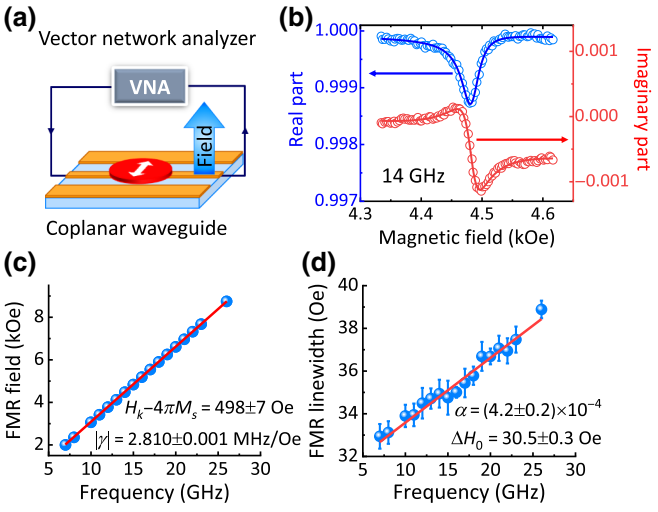

FIG. 6. Vector network analyzer ferromagnetic resonance measurements on YIG thin films grown on GSGG substrates. (a) Experimental configuration. (b) Representative transmission coefficient (S_{21}) profiles, (c) FMR field as a function of microwave frequency (f), and (d) FMR linewidth as a function of f, measured on an 8-nm-thick YIG film. In (b)−(d), the symbols show the experimental data, while the curves and lines show numerical fits.

(v) Plot $H_{\rm FMR}$ vs f and then numerically fit the data using the Kittel equation

$$f = |\gamma|(H_{\rm FMR} + H_k - 4\pi M_s), \tag{9}$$

as shown in Fig. 6(c). Note that in Fig. 6(c), the symbols show the data, while the line shows the fit. The fitting yields two values, $|\gamma|$ and $(H_k - 4\pi M_s)$, as indicated in Fig. 6(c).

(vi) Plot ΔH vs f and then numerically fit the data using

$$\Delta H = \frac{2\alpha}{|\gamma|} f + \Delta H_0 \tag{10}$$

as shown in Fig. 6(d). In Eq. (10), α is the effective damping constant, and ΔH_0 denotes line broadening due to the spatial inhomogeneity of the YIG thin film. Note that in Fig. 6(d), the symbols show the data, while the line shows the fit. The fitting yields α and ΔH_0, as indicated in Fig. 6(d).

Two notes should be made about the FMR data shown in Fig. 6. First, the FMR profiles shown in Fig. 6(b) are obtained after averaging over five field-swept measurements. Second, only the ΔH data over 7–26 GHz are analyzed; the FMR measurements are also carried out at lower frequencies, but ΔH does not follow the linear trend shown in Fig. 6(d) and increases with a decrease in f. This linewidth enhancement at low frequencies results from the so-called "low-field loss" associated with demagnetization effects in not fully saturated films or propagation of "slow" electromagnetic waves along interfaces between magnetic thin films and nonmagnetic substrates [39–41].

Table III presents the data obtained through the above steps. The first column lists the thicknesses (t) of the PMA YIG films. The second column gives the $H_k - 4\pi M_s$ values, which are obtained from the numerical fitting such as that shown in Fig. 6(c). The third and fourth columns give the α and ΔH_0 values, respectively, obtained from the fitting such as that shown in Fig. 6(d).

One can see three important results from the data in Table III. First, the films with $t = 6$–12 nm all exhibit

TABLE III. VNA FMR data of PMA YIG thin films grown on GSGG substrates.

Thickness t (nm)	H_k-4πM_s (Oe)	Damping constant α ($\times 10^{-3}$)	Inhomogeneity line broadening ΔH_0 (Oe)
4	234.4 ± 1.3	1.16 ± 0.02	10.4 ± 0.2
6	511.0 ± 2.1	0.47 ± 0.06	41.4 ± 0.6
7	372.4 ± 0.2	0.45 ± 0.09	13.6 ± 0.6
8	498.4 ± 7.1	0.42 ± 0.02	30.6 ± 0.3
12	440.8 ± 2.8	0.73 ± 0.02	39.1 ± 0.4

relatively low damping, with $\alpha < 0.001$. The 4-nm film shows the largest damping, which is likely because the film has relatively low quality due to lattice mismatching and diffusion at the YIG/GSGG interface, as discussed in Sec. III. Second, $H_k - 4\pi M_s$ is positive for all the films, which confirms the presence of strong PMA in the films. Third, there exists a correlation between $H_k - 4\pi M_s$ and ΔH_0, namely, that the films with low $H_k - 4\pi M_s$ values also exhibit low ΔH_0 values, vice versa. This suggests that the line broadening is mostly due to the spatial inhomogeneity of H_k, rather than $4\pi M_s$, in the YIG films.

Two notes should also be made about the data in Table III. (1) The $H_k - 4\pi M_s$ values in Table III do not match those calculated using the data in Table II. The major reason for this mismatching lies in the fact that the GSGG substrates for the YIG films cited in the two tables are obtained from different sources and thereby show different lattice constants, resulting in a difference in the strength of lattice mismatching-produced strain in the YIG films. Other possible reasons include errors in the field measurements and field misalignments during the measurements. (2) The 6-nm, 7-nm, and 8-nm films show very similar α values, but the 12-nm film shows a value that is about 60% higher. The reason for this difference is currently unknown.

Table IV compares the lowest α value in Table III with the α values of other PMA thin films reported previously [42–50]. These values are all measured with OOP fields, namely, $\theta_H = 0$. The OOP field configuration is taken for two considerations: (1) as mentioned in Sec. IV, two-magnon scattering is prohibited in the presence of an OOP field, but it can occur and contribute to ΔH, and thereby complicate the FMR data analysis if the field is not perpendicular to the film plane [31–34]; and (2) the OOP configuration is relevant for most device applications of magnetic films with perpendicular anisotropy.

It is evident from the data in Table IV that the PMA YIG films have a damping constant lower than other PMA films. This observation clearly suggests the merit of PMA YIG films for applications where low damping is essential. Specifically, α in the PMA YIG film is more than 20 times smaller than that in (Co, Fe)B thin films [46] and more than 40 times smaller than that in $(Co/Ni)_n$ superlattices [45]. Note that (Co, Fe)B and $(Co/Ni)_n$ films are both among the most common PMA thin films in previous studies.

TABLE IV. Summary of the damping constants (α) of PMA thin films reported previously.

Material	Damping constant	Reference
CoGd	0.1	[42]
Co	0.13	[43]
Co_2FeAl	0.008	[44]
$(Co/Ni)_n$	0.02	[45]
(Co, Fe)B	0.011	[46]
$Eu_3Fe_5O_{12}$	0.024	[47]
$Tm_3Fe_5O_{12}$	0.013	[48]
$Tm_3Fe_5O_{12}$	0.02	[49]
$Dy_{3-x}Ce_xFe_{5-y}Al_yO_{12}$	0.23	[50]
$Y_3Fe_5O_{12}$	0.00042	This work

Two points should be mentioned about the data shown in Table IV. First, the table serves to provide an overview of the damping properties of various PMA thin films in recent studies, and a rigorous comparison of the listed α values may be inappropriate because the actual α value also depends on (1) the FMR measurement technique, and (2) the data-analysis approach, in particular, when multiple peaks appear in the FMR profiles. Second, a recent article reported $\alpha = 3 \times 10^{-4}$ for a Bi-doped YIG PMA film [51], which is not included in Table IV. This α value is obtained only for a particular field angle, which is $\theta_H \approx 60°$; in the presence of an OOP field, the film shows $\Delta H \approx 1600$ Oe ($\Delta H_{pp} \approx 950$ Oe), which is notably larger than many of the values reported previously for PMA thin films [44–49].

VII. SPIN-ORBIT TORQUE-INDUCED MAGNETIZATION SWITCHING

The above-presented YIG films with both PMA and low damping may find broad applications in spintronic devices. As an example, this section demonstrates spin-orbit-torque- (SOT) induced switching of magnetization in a YIG/Pt bilayered Hall bar device. The purpose of this demonstration is to illustrate the device application possibility of the YIG films described in the prior sections, while the switching mechanism is exactly the same as in previous works on YIG/Pt [15], $BaFe_{12}O_{19}$/Pt [52], and $Tm_3Fe_5O_{12}$/Pt [22] bilayered structures.

Figure 7 shows the experimental configuration and representative experimental data. Figure 7(a) presents a photo of the measurement device and the electrical measurement configuration. The core component is a Hall bar structure made of an YIG(6 nm)/Pt(5 nm) bilayer. The Pt layer is grown on the YIG film by dc sputtering at room temperature. The Hall bar device is fabricated through photolithography and argon ion milling processes. The central area of the Hall bar is 30 μm long and 10 μm wide. The contact leads of the Hall bar are made of a 200-nm-thick Au film; prior to the deposition of the Au film, a 4-nm-thick Ti adhesion layer is deposited. As for the Pt layer, both the Ti and Au layers are grown by dc sputtering at room temperature. The connections to the Au leads are made through wire bonding using Au wires under a microscope.

The configuration shown in Fig. 7(a) allows for the measurement of the Hall resistivity (ρ_H) of the YIG/Pt Hall bar device. Figures 7(b) and 7(c) present the measured ρ_{AHE} vs H hysteresis responses for an OOP field and an IP field, respectively. As discussed in Sec. III, for the OOP configuration, ρ_H has two components, ρ_{OHE} and

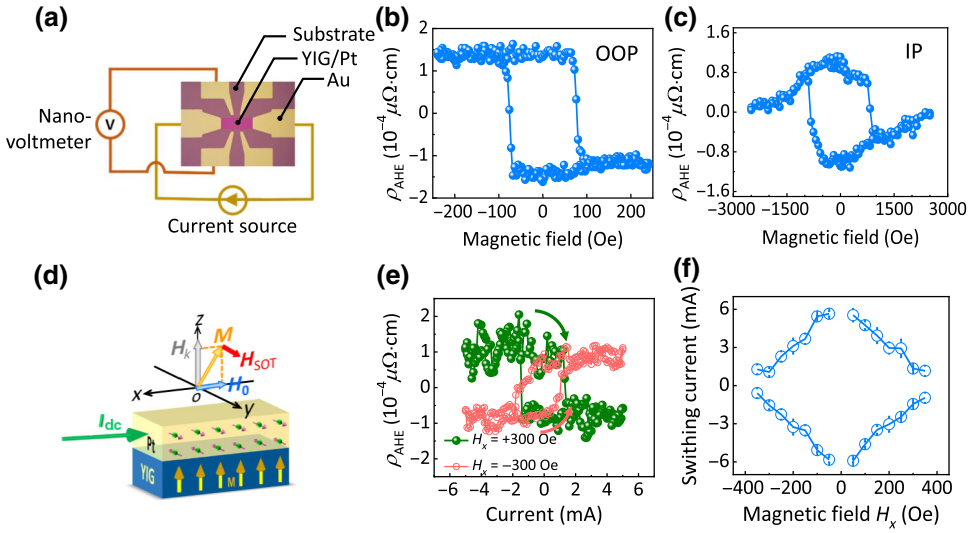

FIG. 7. SOT-induced magnetization switching in a YIG(6nm)/Pt(5 nm) bilayered structure. (a) Experimental configuration. (b) AHE resistivity (ρ_{AHE}) measured as a function of an OOP field using the configuration shown in (a). (c) ρ_{AHE} measured as a function of an IP field using the configuration in (a). (d) Schematic diagram for SOT switching in the YIG/Pt structure. (e) ρ_{AHE} as a function of the dc current (I_{dc}) in the Pt layer for two different external fields (H_x), as indicated. (f) A switching current versus in-plane external-field phase diagram.

ρ_{AHE}. Figure 7(b) shows only ρ_{AHE}; ρ_{OHE} scales linearly with H and has already been subtracted. Figure 7(c) also shows ρ_{AHE} only; ρ_{OHE} is zero in the IP configuration. Note that the data in Fig. 7(b) are the same as those in Fig. 1(d).

The data in Figs. 7(b) and 7(c) clearly show that the AHE response differs for different field configurations. This is because ρ_{AHE} in the Pt layer scales with the perpendicular component ($M_\perp$) of the magnetization in the YIG film. Note that the origin of ρ_{AHE} in the nonmagnetic Pt layer is discussed in Sec. III. In the OOP configuration, a sweep in H results in a switching between $M_\perp > 0$ and $M_\perp < 0$, giving rise to a squarelike loop response shown in Fig. 7(b). In contrast, in the IP configuration, $|M_\perp|$ takes the maximum when $H = 0$, due to PMA, but it gradually reduces to zero when the IP field is increased and gradually rotates the magnetization vector from the perpendicular direction to the plane of the YIG film, giving rise to a distorted loop with $\rho_{AHE} \approx 0$ at high fields, as shown in Fig. 7(c). Note that the fields at which ρ_{AHE} takes zero in Fig. 7(c) are almost the same as the fields at which the magnetization takes the saturation value in Fig. 1(c). Thus, it is evident that one can probe the magnetization status in the YIG film, namely, $M_\perp > 0$ vs $M_\perp < 0$, by simply measuring ρ_{AHE} in the Pt layer.

Figure 7(e) presents the ρ_{AHE} data that demonstrate current-induced magnetization switching. The data are measured as a function of a dc current (I_{dc}) applied to the Pt layer of the Hall bar. The duration of the dc current is 1 ms. Right after the dc current is switched off, a small alternating current of 0.4 mA is applied to the Hall bar and a Hall voltage is measured, using the measurement configuration shown in Fig. 7(a). During the measurements, an IP field is applied along the x axis. This field (H_x) serves to ensure deterministic switching, as in previous work [22,52–54]. The field also assists SOT switching, as discussed shortly. The two sets of data in Fig. 7(e) are obtained with opposite H_x fields, as indicated.

The data in Fig. 7(e) clearly show that a sweep in I_{dc} leads to a flip in the sign of ρ_{AHE}, which indicates current-induced magnetization switching. The data also show that the hysteresis loop evolves in an opposite manner when the IP field (H_x) flips its sign. This result has been observed previously and is a common feature of the SOT switching [22,52–54].

The switching mechanism is illustrated schematically in Fig. 7(d). As a charge current flows in the Pt layer, it generates via the spin Hall effect [55,56] a pure spin current that flows along the Pt thickness direction or the z axis and is polarized along the y axis. This spin current in the Pt layer can transfer spin into the YIG film via so-called s-d exchange interactions at the YIG/Pt interface. The net effect is a torque, often called a SOT, and a corresponding effective field ($\mathbf{H}_{SOT}$) that exert on the magnetization vector ($\mathbf{M}$) in the YIG film and switch it between the up and down directions. For the diagram shown in Fig. 7(d), $\mathbf{M}$ is initially pointing up; the SOT field, with the help of the external field ($\mathbf{H}_0$), rotates $\mathbf{M}$ from the up direction to the down direction, resulting in a switching of $\mathbf{M}$. This switching manifests itself as a change in the sign of ρ_{AHE}, as shown in Fig. 7(e).

Based on the ρ_{AHE} data in Fig. 7(e), one can also determine the switching current, which is about 1.35 mA. This current corresponds to a current density of about 4.5 MA/cm^2. Previous works reported current densities of 10.9 MA/cm^2 for $BaFe_{12}O_{19}$/Pt [52], 18 MA/cm^2 for $Tm_3Fe_5O_{12}$/Pt [22], and 30 MA/cm^2 for YIG/Pt [15]. A rigorous comparison of these switching current densities is not very meaningful as the switching current strongly depends on the strength of PMA in the magnetic layer, the thicknesses of the magnetic and Pt layers, and the magnitude of the IP field (H_x), but the fact that those densities share the same order of magnitude indicates that the interfacial spin transfer in the YIG/Pt system in this work is as efficient as in the bilayered systems reported previously [15,22,52].

Figure 7(f) gives the switching phase diagram where the vertical and horizontal axes show the switching current and the IP field, respectively, both along the x axis, as shown in Fig. 7(d). The data are obtained through the switching measurements similar to those described above for the data in Fig. 7(e). This phase diagram tells the charge current (or the magnetic field) required to switch **M** in the YIG film when a constant field (or a constant current) is applied. Note that each point in Fig. 7(f) shows the average over ten measurements, and the error bars in Fig. 7(f) show the corresponding uncertainties for the averaging. One can see that if a higher field is applied, a smaller current is required to realize the switching. This is consistent with the above-described switching mechanism.

Several remarks should be made about the SOT switching presented in Fig. 7. First, it is believed that the above-discussed switching is realized through domain-wall motion, rather than magnetization rotation, as in previous switching studies [22,52,54]. This is because the device dimension ($30\,\mu\text{m} \times 10\,\mu\text{m}$) is relatively large. Future work is of interest that uses a MOKE microscopy technique [57–59] to confirm this. Second, it is generally accepted that the damping of a PMA film does not affect the current density needed for SOT-induced rotational magnetization switching in the PMA film. In this work, however, the damping is relevant because the switching is realized through domain nucleation and domain-wall motion, as mentioned above. Third, the ρ_{AHE} values in Fig. 7(e) are smaller than those in Fig. 7(b). This observation likely results from the fact that the external field is applied IP for the measurements of the data shown in Fig. 7(e) but is applied OOP for the measurements of the data in Fig. 7(b). Finally, the switching response shown in Fig. 7(e) for $H_x = -300$ Oe seems to be less sharp than that for $H_x = 300$ Oe. This difference is unexpected, and one possible reason is that the AHE in the YIG/Pt bilayer is weak and the AHE signals are noisy.

VIII. CONCLUSIONS AND OUTLOOK

In summary, this work demonstrates the feasibility of development of YIG thin films that are nm thick, exhibit strong PMA, show nearly square magnetic hysteresis loops, and have a damping constant lower than other PMA thin films.

The films in the 4–9-nm thickness range showed (1) smooth surfaces, with a rms surface roughness of about 0.12 nm, (2) strong PMA, with an effective PMA field in the range of 2400–3400 Oe, and (3) squarelike hysteresis loops, with a remnant-to-saturation magnetization ratio in the range of 86%–98%. The growth of a heavy-metal layer on the top of a YIG film and pattering of mm-sized YIG films into μm-sized elements did not result in the degradation of PMA in the film.

The comparison of the structural and magnetic properties of the PMA YIG films with those of the control samples clearly indicates that the PMA originates mainly from magnetoelastic anisotropy associated with a compressive strain along the film thickness direction; such a strain is induced by the lattice mismatching between the YIG films and the GSGG substrates. There exists also cubic magnetocrystalline anisotropy in the YIG films, but its contribution to the PMA is considerably smaller than the strain-induced magnetoelastic anisotropy.

The films showed a damping constant (α) lower than other PMA thin films. For the films with a thickness of 6–8 nm, α ranges from $(4.2 \pm 0.2) \times 10^{-4}$ to $(4.7 \pm 0.6) \times 10^{-4}$. These values represent the lowest damping constants measured on magnetic nm-thick films with perpendicular anisotropy under perpendicular fields.

Current-induced switching of the magnetization in PMA YIG thin films is realized with a YIG/Pt Hall bar structure. The switching makes use of a SOT that is produced through the spin Hall effect in the Pt layer. This work demonstrates the feasibility of the use of spin currents in a neighboring material, such as a heavy metal or a topological insulator, to manipulate the magnetization in PMA YIG films.

The low-damping PMA YIG films demonstrated in this work may have important applications in spintronic devices. It should be highlighted that the films are deposited by sputtering, which is an industry-friendly thin-film growth technique. In terms of potential device applications of PMA YIG films, the following future works are of great, immediate interest. (1) Optimization of the growth processes for the realization of PMA YIG films with even lower damping. A recent work demonstrates the development of nm-thick YIG films with sputtering that showed a damping constant as low as about 5.2×10^{-5} [60], which indicates the possibility of sputtering growth of PMA YIG films with $\alpha < 4.2 \times 10^{-4}$. (2) Measurements of speed of SOT-induced domain-wall motion in PMA YIG thin films. In general, the speed of domain-wall motion is inversely proportional to α [61], so domain walls in YIG thin films are expected to move faster than in other PMA thin films. This work is of significance for the development of racetrack memory. (3) SOT-induced precessional motion or switching of magnetization in nanoscale PMA YIG elements with single domains. Such studies will provide important implications for potential applications of PMA YIG films in spin-torque nano-oscillators and STT memory.

ACKNOWLEDGMENTS

Work at CSU is supported by the U.S. National Science Foundation under Grants No. EFMA-1641989 and No. ECCS-1915849. Work at UW is supported by the U.S. National Science Foundation under Grant No. DMR-1710512. Work at NJU was supported by the National Natural Science Foundation of China under Grants No. 11734006 and No. 11974165.

[1] R. Skomski, P. Manchanda, P. Kumar, B. Balamurugan, A. Kashyap, and D. J. Sellmyer, Predicting the future of permanent-magnet materials, IEEE Trans. Magn. **49**, 3215 (2013).

[2] Z. Chao, K. Zhu, S. C. De Freitas, J. Y. Chang, J. E. Davies, P. Eames, P. P. Freitas, O. Kazakova, C. Kim, C. W. Leung, and S. H. Liou, Magnetoresistive sensor development roadmap (non-recording applications), IEEE Trans. Magn. **55**, 30 (2019).

[3] A. Silva, D. Leitao, M. Silva, P. Ribeiro, F. Franco, P. P. Freitas, and S. Cardoso, in *Condensed Matter Physics National Conference* (2019), pp. 18.

[4] T. Endoh, H. Koike, S. Ikeda, T. Hanyu, and Hideo Ohno, An overview of nonvolatile emerging memories—spintronics for working memories, IEEE J. Emerg. Sel. Topics Circ. Syst. **6**, 109 (2016).

[5] S. Bhatti, R. Sbiaa, A. Hirohata, H. Ohno, S. Fukami, and S. N. Piramanayagam, Spintronics based random access memory: A review, Mater. Today **20**, 530 (2017).

[6] S. Parkin and S. H. Yang. Memory on the racetrack, Nat. Nanotechnol. **10**, 195 (2015).

[7] T. Chen, R. K. Dumas, A. Eklund, P. K. Muduli, A. Houshang, A. A. Awad, P. Dürrenfeld, B. G. Malm, A. Rusu, and J. Åkerman. Spin-torque and spin-Hall nano-oscillators, Proc. IEEE **104**, 1919 (2016).

[8] A. Hirohata, H. Sukegawa, H. Yanagihara, I. Žutić, T. Seki, S. Mizukami, and R. Swaminathan, Roadmap for emerging materials for spintronic device applications, IEEE Trans. Magn. **51**, 1 (2015).

[9] D. Sander, S. O. Valenzuela, D. Makarov, C. H. Marrows, E. E. Fullerton, P. Fischer, J. McCord, P. Vavassori, S. Mangin, P. Pirro, B. Hillebrands, A. D. Kent, T. Jungwirth, O. Gutfleisch, C. G. Kim, and A. Berger, The 2017 magnetism roadmap, J. Phys. D: Appl. Phys. **50**, 363001 (2017).

[10] M. Sparks, *Ferromagnetic-Relaxation Theory* (McGraw Hill, New York, 1964).

[11] Y. Sun and M. Wu, Yttrium iron garnet nano films: Epitaxial growth, spin-pumping efficiency, and Pt-capping-caused damping, Solid State Phys. **64**, 157 (2013. Academic Press, Burlington.

[12] H. Wang, C. Du, P. C. Hammel, and F. Yang, Strain-tunable magnetocrystalline anisotropy in epitaxial $Y_3Fe_5O_{12}$ thin films, Phys. Rev. B **89**, 134404 (2014).

[13] J. Fu, M. Hua, X. Wen, M. Xue, S. Ding, M. Wang, P. Yu, S. Liu, J. Han, C. Wang, H. Du, Y. Yang, and J. Yang, Epitaxial growth of $Y_3Fe_5O_{12}$ thin films with perpendicular magnetic anisotropy, Appl. Phys. Lett. **110**, 202403 (2017).

[14] G. Li, H. Bai, J. Su, Z. Z. Zhu, Y. Zhang, and J. W. Cai, Tunable perpendicular magnetic anisotropy in epitaxial $Y_3Fe_5O_{12}$ films, APL Mater. **7**, 041104 (2019).

[15] C. Y. Guo, C. H. Wan, M. K. Zhao, H. Wu, C. Fang, Z. R. Yan, J. F. Feng, H. F. Liu, and X. F. Han, Spin-orbit torque switching in perpendicular $Y_3Fe_5O_{12}$/Pt bilayer, Appl. Phys. Lett. **114**, 192409 (2019).

[16] H. Chang, P. Li, W. Zhang, T. Liu, A. Hoffmann, L. Deng, and M. Wu, Nanometer-thick yttrium iron garnet films with extremely low damping, IEEE Magn. Lett. **5**, 4 (2014).

[17] T. Liu, H. Chang, V. Vlaminck, Y. Sun, M. Kabatek, A. Hoffmann, L. Deng, and M. Wu, Ferromagnetic resonance of sputtered yttrium iron garnet nanometer films, J. Appl. Phys. **115**, 17A501 (2014).

[18] Y. M. Lu, Y. Choi, C. M. Ortega, X. M. Cheng, J. W. Cai, S. Y. Huang, L. Sun, and C. L. Chien, Pt Magnetic Polarization on $Y_3Fe_5O_{12}$ and Magnetotransport Characteristics, Phys. Rev. Lett. **110**, 147207 (2013).

[19] Y. T. Chen, S. Takahashi, H. Nakayama, M. Althammer, S. T. B. Goennenwein, E. Saitoh, and G. E. W. Bauer, Theory of spin Hall magnetoresistance, Phys. Rev. B **87**, 144411 (2013).

[20] S. S. L. Zhang and G. Vignale, Nonlocal Anomalous Hall Effect, Phys. Rev. Lett. **116**, 136601 (2016).

[21] S. Meyer, R. Schlitz, S. Geprägs, M. Opel, H. Huebl, R. Gross, and S. T. Goennenwein, Anomalous Hall effect in YIG|Pt bilayers, Appl. Phys. Lett. **106**, 132402 (2015).

[22] C. O. Avci, A. Quindeau, C. F. Pai, M. Mann, L. Caretta, A. S. Tang, M. C. Onbasli, C. A. Ross, and G. S. Beach, Current-induced switching in a magnetic insulator, Nat. Mater. **16**, 309 (2017).

[23] C. Tang, P. Sellappan, Y. Liu, Y. Xu, J. E. Garay, and J. Shi, Anomalous Hall hysteresis in $Tm_3Fe_5O_{12}$/Pt with strain-induced perpendicular magnetic anisotropy, Phys. Rev. B **94**, 140403 (2016).

[24] E. L. Jakubisova, S. Visnovsky, H. Chang, and M. Wu, Interface effects in nanometer-thick yttrium iron garnet films studied by magneto-optical spectroscopy, Appl. Phys. Lett. **108**, 082403 (2016).

[25] A. Mitra, O. Cespedes, Q. Ramasse, M. Ali, S. Marmion, M. Ward, R. M. D. Brydson, C. J. Kinane, J. F. K. Cooper, S. Langridge, and B. J. Hickey, Interfacial origin of the magnetisation suppression of thin film yttrium iron garnet, Sci. Rep. **7**, 1 (2017).

[26] J. F. K. Cooper, C. J. Kinane, S. Langridge, M. Ali, B. J. Hickey, T. Niizeki, K. Uchida, E. Saitoh, H. Ambaye, and A. Glavic, Unexpected structural and magnetic depth dependence of YIG thin films, Phys. Rev. B **96**, 104404 (2017).

[27] J. M. Gomez-Perez, S. Vélez, L. McKenzie-Sell, M. Amado, J. Herrero-Martín, J. López-López, S. Blanco-Canosa, L. E. Hueso, A. Chuvilin, J. W. Robinson, and F. Casanova, Synthetic Antiferromagnetic Coupling Between Ultrathin Insulating Garnets, Phys. Rev. Appl. **10**, 044046 (2018).

[28] The polarized neutron reflectometry measurements on YIG thin films grown under the same conditions indicate an interfacial layer of about 5 nm thick. At room temperature, the magnetization across the thickness of this interfacial layer increases from about zero (at the interface with the substrate) to the bulk value of the YIG in the presence of a magnetic field of about 5 kOe. The detailed results will be reported in a separate paper.

[29] L. Lu, Z. Wang, G. Mead, C. Kaiser, Q. Leng, and M. Wu, Damping in free layers of tunnel magneto-resistance readers, Appl. Phys. Lett. **105**, 012405 (2014).

[30] D. Richardson, S. Katz, J. Wang, Y. K. Takahashi, K. Srinivasan, A. Kalitsov, K. Hono, A. Ajan, and M. Wu, Near-T_c Ferromagnetic Resonance and Damping in Fe Pt-Based Heat-Assisted Magnetic Recording Media, Phys. Rev. Appl. **10**, 054046 (2018).

[31] R. D. McMichael and P. Krivosik, Classical model of extrinsic ferromagnetic resonance linewidth in ultrathin films, IEEE Trans. Magn. **40**, 2 (2014).

[32] P. Krivosika, N. Mo, S. Kalarickalb, and C. E. Patton, Hamiltonian formalism for two magnon scattering microwave relaxation: Theory and applications, J. Appl. Phys. **101**, 083901 (2007).

[33] S. S. Kalarickal, P. Krivosik, J. Das, K. S. Kim, and C. E. Patton, Microwave damping in polycrystalline Fe-Ti-N films: Physical mechanisms and correlations with composition and structure, Phys. Rev. B **77**, 054427 (2008).

[34] L. Lu, J. Young, M. Wu, C. Mathieu, M. Hadley, P. Krivosik, and N. Mo, Tuning of magnetization relaxation in ferromagnetic thin films through seed layers, Appl. Phys. Lett. **100**, 022403 (2012).

[35] K. M. Krishnan, *Fundamentals and Applications of Magnetic Materials* (Oxford University Press, Oxford, England, 2016).

[36] W. H. Von Aulock, *Handbook of Microwave Ferrite Materials* (Academic, London, 1965).

[37] Y. Ding, T. J. Klemmer, and T. M. Crawford, A coplanar waveguide permeameter for studying high-frequency properties of soft magnetic materials, J. Appl. Phys. **96**, 2969 (2004).

[38] H. T. Nembach, T. J. Silva, J. M. Shaw, M. L. Schneider, M. J. Carey, S. Maat, and J. R. Childress, Perpendicular ferromagnetic resonance measurements of damping and landé g - factor in sputtered $(Co_2Mn)_{1-x}Ge_x$ thin films, Phys. Rev. B **84**, 054424 (2011).

[39] D. Polder and J. Smit, Resonance phenomena in ferrites, Rev. Mod. Phys. **25**, 89 (1953).

[40] E. Schloemann, Low-frequency losses in ferrite microwave devices, unpublished.

[41] Sangita S. Kalarickal, Nan Mo, and Pavol Krivosik, And Carl E. Patton, ferromagnetic resonance linewidth mechanisms in polycrystalline ferrites: Role of grain-to-grain and grain-boundary two-magnon scattering processes, Phys. Rev. B **79**, 094427 (2009).

[42] M. Binder, A. Weber, O. Mosendz, G. Woltersdorf, M. Izquierdo, I. Neudecker, J. R. Dahn, T. D. Hatchard, J.-U. Thiele, C. H. Back, and M. R. Scheinfein, Magnetization dynamics of the ferrimagnet CoGd near the compensation of magnetization and angular momentum, Phys. Rev. B **74**, 134404 (2006).

[43] A. J. Schellekens, L. Deen, D. Wang, J. T. Kohlhepp, H. J. M. Swagten, and B. Koopmans, Determining the gilbert damping in perpendicularly magnetized $Pt/Co/AlO_x$ films, Appl. Phys. Lett. **102**, 082405 (2013).

[44] Y. Cui, B. Khodadadi, S. Schäfer, T. Mewes, J. Lu, and S. A. Wolf, Interfacial perpendicular magnetic anisotropy and damping parameter in ultra thin Co_2FeAl films, Appl. Phys. Lett. **102**, 162403 (2013).

[45] H. S. Song, K. D. Lee, J. W. Sohn, S. H. Yang, S. S. P. Parkin, C. Y. You, and S. C. Shin, Observation of the intrinsic Gilbert damping constant in Co/Ni multilayers independent of the stack number with perpendicular anisotropy, Appl. Phys. Lett. **102**, 102401 (2013).

[46] D. S. Wang, S. Y. Lai, T. Y. Lin, C. W. Chien, D. Ellsworth, L. W. Wang, J. W. Liao, L. Lu, Y. H. Wang, M. Wu, and C. H. Lai, High thermal stability and low Gilbert damping constant of CoFeB/MgO bilayer with perpendicular magnetic anisotropy by Al capping and rapid thermal annealing, Appl. Phys. Lett. **104**, 142402 (2014).

[47] C. N. Wu, C. C. Tseng, Y. T. Fanchiang, C. K. Cheng, K. Y. Lin, S. L. Yeh, S. R. Yang, C. T. Wu, T. Liu, M. Wu, and M. Hong, High-quality thulium iron garnet films with tunable perpendicular magnetic anisotropy by off-axis sputtering–correlation between magnetic properties and film strain, Sci. Rep. **8**, 11087 (2018).

[48] O. Ciubotariu, A. Semisalova, K. Lenz, and M. Albrecht, Strain-induced perpendicular magnetic anisotropy and Gilbert damping of $Tm_3Fe_5O_{12}$ thin films, Sci. Rep. **9**, 17474 (2019).

[49] J. J. Bauer, E. R. Rosenberg, S. Kundu, K. A. Mkhoyan, P. Quarterman, A. J. Grutter, B. J. Kirby, J. A. Borchers, and C. A. Ross, Dysprosium iron garnet thin films with perpendicular magnetic anisotropy on silicon, Adv. Electron. Mater. **6**, 1900820 (2020).

[50] E. R. Rosenberg, L. Beran, C. O. Avci, C. Zeledon, B. Song, C. Gonzalez-Fuentes, J. Mendil, P. Gambardella, M. Veis, C. Garcia, and G. S. Beach, Magnetism and spin transport in rare-earth-rich epitaxial terbium and europium iron garnet films, Phys. Rev. Mater. **2**, 094405 (2018).

[51] L. Soumah, N. Beaulieu, L. Qassym, C. Carrétéro, E. Jacquet, R. Lebourgeois, J. B. Youssef, P. Bortolotti, V. Cros, and A. Anane, Ultra-low damping insulating magnetic thin films get perpendicular, Nat. Commun. **9**, 1 (2018).

[52] P. Li, T. Liu, H. Chang, A. Kalitsov, W. Zhang, G. Csaba, W. Li, D. Richardson, A. DeMann, G. Rimal, and H. Dey, Spin–orbit torque-assisted switching in magnetic insulator thin films with perpendicular magnetic anisotropy, Nat. Commun. **7**, 1 (2016).

[53] I. M. Miron, K. Garello, G. Gaudin, P. J. Zermatten, M. V. Costache, S. Auffret, S. Bandiera, B. Rodmacq, A. Schuhl, and P. Gambardella, Perpendicular switching of a single ferromagnetic layer induced by in-plane current injection, Nature **476**, 189 (2011).

[54] L. Liu, C. F. Pai, Y. Li, H. W. Tseng, D. C. Ralph, and R. A. Buhrman, Spin-torque switching with the giant spin Hall effect of tantalum, Science **336**, 555 (2012).

[55] J. E. Hirsch, Spin Hall Effect, Phys. Rev. Lett. **83**, 1834 (1999).

[56] A. Hoffmann, Spin Hall effects in metals, IEEE Trans. Magn. **49**, 5172 (2013).

[57] S. A. Siddiqui, J. Han, J. T. Finley, C. A. Ross, and L. Liu, Current-induced Domain Wall Motion in a Compensated Ferrimagnet, Phys. Rev. Lett. **121**, 057701 (2018).

[58] C. O. Avci, E. Rosenberg, L. Caretta, F. Büttner, M. Mann, C. Marcus, D. Bono, D. C, A. Ross, and G. S. Beach, Interface-driven chiral magnetism and current-driven domain walls in insulating magnetic garnets, Nat. Nanotechnol. **14**, 561 (2019).

[59] S. Vélez, J. Schaab, M. S. Wörnle, M. Müller, E. Gradauskaite, P. Welter, C. Gutgsell, C. Nistor, C. L. Degen, M. Trassin, and M. Fiebig, High-speed domain wall racetracks in a magnetic insulator, Nat. Commun. **10**, 1 (2019).

[60] J. Ding, T. Liu, H. Chang, and M. Wu, Sputtering growth of Low-damping yttrium iron garnet thin films, IEEE Magn. Lett. **11**, 5502305 (2020).

[61] R. Wieser, E. Y. Vedmedenko, P. Weinberger, and R. Wiesendanger, Current-driven domain wall motion in cylindrical nanowires, Phys. Rev. B **82**, 144430 (2010).